Published in final edited form as:

Cell Rep. 2022 March 29; 38(13): 110606. doi:10.1016/j.celrep.2022.110606.

Coarse-to-fine processing drives the efficient coding of natural scenes in mouse visual cortex

Rolf Skyberg[1,2], **Seiji Tanabe**[1,2], **Hui Chen**[1], **Jianhua Cang**[1,3,*]

[1]Department of Biology and Department of Psychology, University of Virginia, Charlottesville, VA 22904, USA

[2]These authors contributed equally

[3]Lead contact

SUMMARY

The visual system processes sensory inputs sequentially, perceiving coarse information before fine details. Here we study the neural basis of coarse-to-fine processing and its computational benefits in natural vision. We find that primary visual cortical neurons in awake mice respond to natural scenes in a coarse-to-fine manner, primarily driven by individual neurons rapidly shifting their spatial frequency preference from low to high over a brief response period. This shift transforms the population response in a way that counteracts the statistical regularities of natural scenes, thereby reducing redundancy and generating a more efficient neural representation. The increase in representational efficiency does not occur in either dark-reared or anesthetized mice, which show significantly attenuated coarse-to-fine spatial processing. Collectively, these results illustrate that coarse-to-fine processing is state dependent, develops postnatally via visual experience, and provides a computational advantage by generating more efficient representations of the complex spatial statistics of ethologically relevant natural scenes.

In brief

Skyberg et al. show that the visual cortex of mice processes natural scenes in a coarse-to-fine manner, driven by individual neuron's temporal dynamics. These response dynamics, which require visual experience to develop, reduce redundancy in the neural code and lead to more efficient representations of complex visual stimuli.

Graphical Abstract

*Correspondence: cang@virginia.edu.

AUTHOR CONTRIBUTIONS

R.S., S.T., and J.C. designed the experiments. R.S. performed experiments. R.S. and S.T. analyzed the data with assistance from H.C. R.S. and J.C. wrote the manuscript with feedback from all authors.

SUPPLEMENTAL INFORMATION

Supplemental information can be found online at https://doi.org/10.1016/j.celrep.2022.110606.

DECLARATION OF INTERESTS

The authors declare no competing interests.

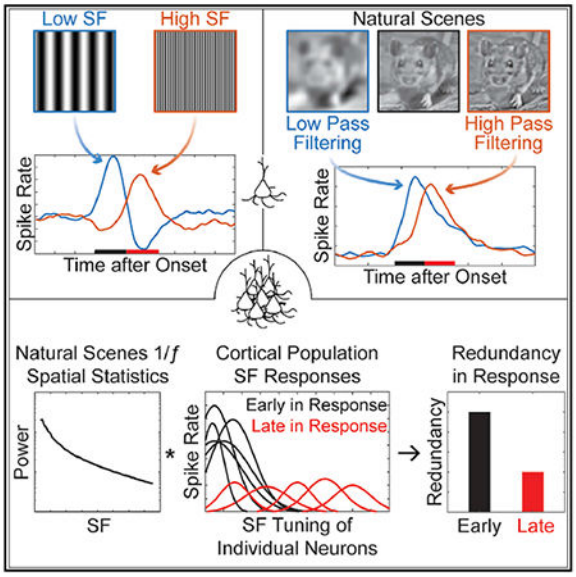

INTRODUCTION

The visual system encodes the rich information of complex environment under the limitations of available biological resources. This notion has led to the proposal that the underlying “neural code“ must be efficient (Atick and Redlich, 1990; Attneave, 1954; Barlow, 1961; Simoncelli and Olshausen, 2001). The efficient coding hypothesis forms the framework to explain many properties of the early visual system, such as asymmetries in the On/Off pathways (Gjorgjieva et al., 2014; Karklin and Simoncelli, 2011; Ratliff et al., 2010), retinal ganglion cell receptive field structure and response decorrelation (Karklin and Simoncelli, 2011; Nirenberg et al., 2001; Pitkow and Meister, 2012; Roy et al., 2021), cortical simple and complex receptive field structure (Karklin and Lewicki, 2009; Olshausen and Field, 1996a), and dimensionality, sparseness, and coding smoothness of certain subcortical and cortical responses (Dan et al., 1996; Kowalewski et al., 2021; Stringer et al., 2019; Vinje and Gallant, 2000).

Importantly, these studies have mostly focused on static visual representations without considering their temporal dynamics. Many visual stimuli of varying complexity have been shown to be processed in a temporally dynamic fashion, with certain aspects of the stimulus being encoded before others. This has been shown at the neuronal level for spatial frequency (SF; Allen and Freeman, 2006; Bredfeldt and Ringach, 2002; Cai et al., 1997; Chen et al., 2018; Frazor et al., 2004; Mazer et al., 2002;Vreysen et al., 2012), orientation (Ringach et al., 1997), direction (Perge et al., 2005), and binocularity (Menz and Freeman, 2003), as well as for complex stimuli like faces (Matsumoto et al., 2005; Sugase et al., 1999). Among these, the most well-established is the dynamic processing of spatial information, where individual cells rapidly shift their SF preference from low to high during a brief response period (Allen and Freeman, 2006; Bredfeldt and Ringach, 2002; Cai et al., 1997; Chen et al., 2018; Frazor et al., 2004; Mazer et al., 2002; Vreysen et al., 2012). However, whether

and how coarse-to-fine processing contributes to efficient coding, and more generally, the computational benefits it provides, remain unknown.

Neural codes are most efficient when responses are uncorrelated and the representations are of high dimension (Atick and Redlich, 1990; Barlow, 1961; Simoncelli and Olshausen, 2001; Stringer et al., 2019). One way to achieve this efficiency is by eliminating responses to statistical regularities of the encoded inputs (Barlow, 1961). A prominent statistical regularity in natural scenes is the $1/f$ relationship between SF and spectral power (Olshausen and Field, 1996b; Ruderman and Bialek, 1994; Simoncelli and Olshausen, 2001). Thus, coarse-to-fine SF processing could, in theory, produce more efficient neural representations by shifting neural responses away from the high-power, low-SF components within natural scenes.

In this study, we test the above prediction by measuring the spatiotemporal receptive fields of neurons in the mouse primary visual cortex (V1) in response to simple grating stimuli, and by determining the efficiency of the neural representation of complex natural scenes. We find that the vast majority of V1 neurons in awake mice respond to gratings in a coarse-to-fine fashion, showing two temporally offset peaks to low and high SFs that generate a rapid flattening of the population SF tuning curve. Excitingly, V1 neurons also show coarse-to-fine processing of natural scenes, which drives a substantial and significant increase in the representational efficiency of these complex stimuli. We further demonstrate that coarse-to-fine SF processing develops postnatally via visual experience and is significantly attenuated in anesthetized mice. Together, our work unveils a computational advantage for temporally dynamic cortical responses in efficiently representing the ethologically relevant natural stimuli that the visual system evolved and developed to encode.

RESULTS

Coarse-to-fine processing in awake mouse V1

We performed large-scale physiological recordings from awake mice to determine the temporal dynamics of how individual V1 neurons process spatial information. First, using rapidly displayed gratings and subspace forward correlation (Figure 1A; see STAR Methods), we revealed two distinct types of spatiotemporal receptive fields (STRFs). The first type was one in which the peak responses to all SFs occurred around the same time (Figure 1B) and made up ~25% of the V1 population in awake mice (n = 64/259). Most of these “one-peak cells” responded maximally between 80 and 110 ms (Figure 1D) and preferred low SFs (Figure S2C). The second type was one that responded to low SFs faster than to high SFs, resulting in a dramatic shift of SF preference from low to high (i.e., from coarse to fine) during their response trajectory (Figure 1C). The SF shift was often large and abrupt, generating two distinct peaks in the SF response profile. Such “two-peak cells” made up a vast majority of the awake V1 population (75.3%, n = 195/259). At their first peak (i.e., τ_{pk1}), the STRFs of these two-peak cells were similar to one-peak cells in both the latency (Figure 1D) and SF preference (Figures S2A and S2C). In contrast, at the second temporally delayed peak (i.e., τ_{pk2}), the SF preferences were much higher and more diverse than at the first peak, covering the entire range of tested SFs (Figures 2B and S2B). Nearly

every two-peak cell (94.4%, n = 184/195) shifted in a coarse-to-fine fashion from τ_{pk1} to τ_{pk2} (Figures 2B and S2D).

We found that the magnitude of SF shift (Δf_{pk}; mean of 1.64 octaves, i.e., a tripling of SF preference; and median of 2.00 octaves, i.e., a quadrupling of SF preference) was much greater than what has been previously reported for anesthetized mice (mean of 0.85 octaves; Vreysen et al., 2012) and anesthetized non-human primates (mean of 0.62 octaves; Bredfeldt and Ringach, 2002). We therefore tested the influence of anesthesia and found it had multiple effects on V1 coarse-to-fine SF processing. First, anesthesia significantly attenuated the average percentage of two-peak cells, from 75.8% (±3.4) in awake V1 to 51.6% (±5.2) in anesthetized V1 ($p = 0.002$, z statistic = 3.12, Mann-Whitney test; Figure 2A). Second, even among the remaining two-peak cells, the average Δf_{pk} was significantly reduced during anesthesia (from 2.17 to 0.90 octaves; p = 2.56e-18, z statistic = 8.73, Mann-Whitney test; Figures 2B and S2D). Collectively, the average Δf_{pk} from anesthetized mice was significantly lower than that of awake mice (from mean of 1.63 (±0.11) to 0.47 (±0.10) octaves; $p = 5.4e^{-5}$, z statistic = 4.038, Mann-Whitney test; Figure 2C). Furthermore, we found that one-peak cells, at the population level, also processed SF information in a coarse-to-fine manner, with those that preferred high SFs tending to respond at longer latencies than those preferring low SFs (Figure S2F). This trend disappeared in anesthetized mice. In other words, anesthesia selectively diminished the high SF responses of one- and two-peak cells, thereby attenuating cortical coarse-to-fine processing as a whole.

To determine how coarse-to-fine SF processing of individual cells affects the SF tuning of the cortical population, we calculated the average SF responses of all V1 cells at six distinct latencies (Figure 2D). Between 60 and 120 ms, the cortical representation of SF information shifted in a coarse-to-fine manner, evolving from low pass to largely flat and eventually to more high pass (Figure 2D). Between 105 and 120 ms the low-SF population responses became negative, indicative of temporally delayed suppression at low SFs (Allen and Freeman, 2006; Bredfeldt and Ringach, 2002). Conversely, anesthetized mice with significantly attenuated cellular coarse-to-fine processing displayed little to no shift in their population SF tuning, instead remaining low pass throughout the duration of the response (Figure 2E). Additionally, there were no signs of temporally delayed, low-SF suppression in the anesthetized population response. Finally, we calculated the average time-integrated SF tuning curves of the awake (blue) and anesthetized (gray) V1 populations (Figure 2F). The time-integrated SF tuning curves were substantially different between awake and anesthetized mice, particularly in regard to the medium to high SFs (Figure 2F). Collectively, these data directly demonstrate that coarse-to-fine SF processing is state dependent and in awake mice acts to dynamically shift cortical SF tuning away from a low-pass representation.

Awake mice process natural scenes in a coarse-to-fine manner

We next asked whether the coarse-to-fine processing of SF information seen in response to simple and artificial gratings occurred while viewing ethologically relevant stimuli, like natural scenes (Figure 3A). Natural scenes are high-dimensional stimuli containing a wide range of SFs and varying noticeably from one scene to the next. Despite this variability,

the SF statistics of natural scenes all tend to obey a $1/f$ relationship between SF and spectral power (Figure 3B, black; Olshausen and Field, 1996b; Ruderman and Bialek, 1994; Simoncelli and Olshausen, 2001). To test if awake mice process the spatial statistics of natural scenes in a coarse-to-fine manner, we generated two variants of 60 different natural scenes, low-pass filtered and high-pass filtered (Figure 3A). Low-pass or high-pass filtering of natural scenes attenuates the high-SF or low-SF information they contain, respectively (Figures 3A and 3B). If natural scenes are processed in a coarse-to-fine fashion, V1 neurons should respond to low-pass filtered scenes (with attenuated high-SF components) more quickly than to high-pass ones (with attenuated low-SF components). This prediction held true at both the level of individual neurons (Figures 3C–3F and S3A–S3D) and across the population (Figures 3G and 3H), with responses to low-pass scenes reaching their peaks before high-pass natural scene responses. In fact, nearly every cell we recorded (92.3%, n = 159/171; 5 mice) responded more quickly to low-pass natural scenes than they did to high-pass ones (Figure 3I), with an average difference of 23.8 ± 1.67 ms. Furthermore, the differences in peak response times between low-pass and high-pass natural scenes were not correlated with the response magnitude (Figure S3H). In other words, the differences in response latency are not due to differences in response strength, but in fact reflect sequential processing of the natural scenes.

Using subspace forward correlation, we were able to map the STRFs of 116 of the 171 neurons that responded to the filtered natural scenes. Both one-peak cells (n = 32, Figure S3E) and two-peak cells (n = 84, Figure S3F) showed similar temporal progressions to the filtered natural scenes, responding more quickly to low-pass filtered scenes than high-pass filtered scenes (Figures S3E–S3G). Interestingly, the average normalized responses of two-peak cells to all variants of natural scenes were substantially larger than that of one-peak cells (Figures S3E–S3G), suggesting that two-peak cells contribute more strongly to natural scene responses. This was particularly true with the high-pass filtered natural scene responses between one- and two-peak cells (Figures S3E and S3F). Collectively, these data illustrate that the spatial statistics of natural scenes are processed in a coarse-to-fine manner in mouse V1 and that both one- and two-peak cells contribute, albeit differently, to this temporally dynamic processing.

Coarse-to-fine processing reduces redundancy within the neural representation of natural scenes

The discovery that coarse-to-fine spatial processing occurs when viewing high-dimensional, ethologically relevant, natural scenes raises important questions regarding the computational advantages this process may provide visual processing. One compelling hypothesis is that it may reduce redundancies within the neural representation of natural scenes. To test this hypothesis directly we recorded the responses of 629 V1 neurons, from eight adult awake mice, to 20 repeats of 150 unfiltered natural scenes. Note that we increased the number of natural scenes and removed filtered variants for this particular experiment. The recorded responses were then averaged across repeats and analyzed by principal component analysis (PCA). The intuition behind the following analyses is graphically represented in Figure 4A. In a hypothetical scenario of two neurons that respond identically to each other, their responses would be perfectly redundant (Figure 4A top, black squares). This redundant

neural code would generate a long and narrow natural scene response manifold in this two-dimensional space (Figure 4A top, black dotted line), which can be captured by one large principal component (PC) (PC1, along y = x) and one small PC (PC2, orthogonal to y = x). In this example, the percentage of the total variance described by PC1 and PC2 would be nearly 100% and 0%, respectively, and the resulting eigenspectrum slope would be steep (Figure 4A bottom, black). On the other extreme, if both neurons generate unique responses, the redundancy between their responses would be low (Figure 4A top, red circles). This hypothetical neural code, having similar PC1 and PC2 (roughly 50% for each) and a flat eigenspectrum slope, would be considered efficient under the efficient coding hypothesis (Barlow, 1961). Thus, the slope of the eigenspectrum, the number of PCs required to explain the neural response manifold, and the percentage of total variance explained by PC1 are all indications how redundant or efficient a neural representation is.

To measure if redundancy in the neural representation of natural scenes from V1 of awake mice changed over the response, we began by combining all our data into a single group (n = 629, eight mice). We chose the time points where PC1 reached its local maximum within an early temporal window that reflects “coarse” processing of natural scenes (100–150 ms; $\tau 1$ =121 ms; solid line in Figures 4B–4D) and within a later temporal window that reflects “fine” processing of natural scenes (151–225 ms; $\tau 2$ = 165 ms; dotted line in Figures 4B–4D). We chose these temporal windows based on the average population responses to low-pass and high-pass natural scenes (Figures 3G and 3H; see STAR Methods). Comparing the average firing rate between these two time points (Figure 4B, solid and dotted lines) shows similar population responses at both times, making it unlikely that any subsequent findings are due simply to wholesale changes in the responsivity of the population. Plotting the eigenspectrum at $\tau 1$ and $\tau 2$ (Figure 4D, solid and dotted lines, respectively) revealed a clear and substantial flattening of the eigenspectra over time. From $\tau 1$ to $\tau 2$ the eigenspectrum slope decreased from −0.49 to −0.33, a net change of 0.16 (ΔSlope, positive values indicate flattening; Figure 4D). Additionally, we found that the number of large PCs, that is, the number of PCs that rise above a threshold derived via data shuffling (see STAR Methods), also changed substantially from $\tau 1$ to $\tau 2$ (Figure 4D, inset). At $\tau 1$ the first 26 PCs were greater than their shuffled counterparts, whereas at $\tau 2$ the first 34 PCs were greater than the shuffled data, an increase of eight PCs (−ΔLarge PCs; Figure 4D, inset). A positive ΔLarge PC indicates that more PCs are required to describe the response manifold at $\tau 2$ compared with $\tau 1$. As a final measure, we calculated the change in the percentage of variance described by PC1 from $\tau 1$ to $\tau 2$. We found an almost 2-fold decrease (from 6.28% to 3.31%, Figure 4D), further indicating a flattening of the eigenspectrum over time.

Next, we tested if the redundancy reduction occurred within recordings from individual mice. We chose $\tau 1$ and $\tau 2$ in each animal following the same procedure as described above (Figure 4E). First, we compared the slope of the eigenspectra and found that in every animal the slope flattened from $\tau 1$ to $\tau 2$ and was significantly less negative at $\tau 2$ (−0.39 ± 0.04) than at $\tau 1$ (−0.55 ± 0.05; p = 0.008, Wilcoxon; Figure 4F). The number of large PCs required to explain the response manifold also changed on an animal-to-animal basis and was significantly larger at $\tau 2$ (17.1 ± 1.9) than at $\tau 1$ (12.6 ± 1.4; p = 0.008, Wilcoxon; Figure 4G). Finally, the percentage of total variance described by PC1 was significantly larger at $\tau 1$ (11.33 ± 0.98) than at $\tau 2$ (8.00 ± 0.94; p = 0.008, Wilcoxon; Figure 4H). These

findings were not dependent upon the specific τ2 chosen for each animal (Figures S6G–S6I). Thus, all three measures demonstrate that coarse-to-fine SF processing substantially decreases the redundancy in V1's representation of the spatial statistics of natural scenes.

It is conceivable that the reduction in redundancy in the representation of natural scenes at τ2 could be caused by an increase in the variability of neuronal responses as the influence of the stimulus decays. This could also generate a flatter eigenspectrum at τ2 but would suggest that the responses are overtaken by noise rather than rearranging into a more efficient representation. To test this possibility, we calculated the Fano factor (Churchland et al., 2010), a measure of response variability, of responses over time from a population of 140 cells from three mice that were shown unfiltered natural scenes. We found that the Fano factor was high (~1.3) before the stimulus reached the cortex and quickly decreased toward 1 at the onset of stimulus-evoked activity (Figure S4), similar to previous findings in many brain areas (Churchland et al., 2010). Importantly, the Fano factor remained low and near 1 throughout the duration of the population response (~125–225 ms), excluding the possibility of a disproportional increase in neuronal variability during this period. Thus, the flattening of the natural scene response eigenspectrum at τ2 is indicative of the neuronal representation becoming more efficiently organized.

Coarse-to-fine processing requires visual experience to develop postnatally

The finding that coarse-to-fine SF processing drives efficient coding of natural scenes raises an intriguing possibility that natural viewing during postnatal development may be required for its normal development. To test this, we mapped the STRFs of V1 neurons from postnatal day 17–18 mice ("P17" group, 10 mice; Figure 5A), only a few days after vision onset, and from adult mice that were reared in complete darkness throughout life ("DR," 12 mice; Figure 5A). We found a significant decrease in the average percentage of two-peak cells in P17 mice (48.4% ± 7.2, compared with 75.8% ± 3.4 in adult; $p = 0.0039$, z statistic = 2.89, Mann-Whitney test; Figure 5B). Among the remaining two-peak cells, their Δf_{pk} was also significantly reduced (1.43 ± 0.14 octaves at P17 and 2.17 ± 0.08 octaves in adult; $p = 9.87e^{-6}$, z statistic = 4.42, Mann-Whitney test; Figure S4J). Together, these changes resulted in a significantly lower average Δf_{pk} for all P17 mice (0.83 ± 0.13 octaves) compared with adult mice (1.63 ± 0.11 octaves; $p = 2.45e^{-04}$, z statistic = 3.67, Mann-Whitney test; Figure 5C). These single cell developmental differences led to a substantially reduced time-integrated representation of high-SF information in P17 mice (Figure 5D).

Similar findings were observed in DR mice, which had a smaller average percentage of two-peak cells (60.96% ± 4.3) than adult normal reared mice ($p = 0.024$, z statistic = 2.25, Mann-Whitney test; Figure 5B) and reduced Δf_{pk} among the remaining two-peak cells (1.43 ± 0.12; $p = 2.54e^{-06}$, z statistic = 4.71, Mann-Whitney test; Figure S4J). Similarly, the average Δf_{pk} values for all DR mice (0.84 ± 0.09 octaves) was significantly lower than that of adult normal reared mice ($p = 9.01e^{-5}$, z statistic = 3.92, Mann-Whitney test; Figure 5C). Interestingly, as a population one-peak cells from adult DR mice still showed coarse-to-fine SF processing similar to that of normal reared mice (Figure S5L), suggesting that dark rearing selectively attenuates the coarse-to-fine processing of two-peak cells rather than a

wholesale deterioration of high-SF responses. At the population level, the effects of dark rearing manifested as a substantial attenuation of the medium- to high-SF time-integrated responses (Figure 5D).

Together, these results indicate that both the percentage of two-peak cells, the magnitude of their SF shift, and consequently coarse-to-fine SF processing as a whole, require patterned visual experience to develop properly after vision onset. Importantly, we find that dark rearing had specific and significant effects on the coarse-to-fine SF processing of two-peak cells, while leaving other aspects of cortical SF processing largely unscathed (Kowalewski et al., 2021; Nishio et al., 2021).

Disrupting coarse-to-fine processing reduces efficient coding of natural scenes

The specific deficit seen in the DR mice provided us an opportunity to more directly test the idea that coarse-to-fine processing drives efficient coding, where we tracked the temporal evolution of redundancy within neural representations of natural scenes in these mice. We first combined all cells from DR mice into a single group (n = 312, six mice) and analyzed the data identically to that of the normal reared population, choosing the two time points (τ1 = 124ms, τ2 = 168ms) at which PC1 reached its local maximum within the previously defined temporal windows (Figure S6A). Qualitatively, the DR response eigenspectrum at these two time points were very similar, only showing subtle signs of flattening. Our three quantitative methods confirmed this to be true (Figures S6B and S6C). The same conclusion held true with the analysis of individual DR animals. The eigenspectrum slope across all DR mice at τ1 (−0.50 ± 0.04) was not significantly different from that at τ2 (−0.48 ± 0.03; p = 0.688, Wilcoxon; Figure 6A). The number of large PCs were also similar at τ1 and τ2 (11.3 ± 1.9 and 10.5 ± 1.9 respectively; p = 0.5, Wilcoxon; Figure 6B), and the same was true for the percentage of total variance explained by PC1 (12.14% ± 1.60% at τ1 versus 11.47% ± 1.10% at τ2; p = 0.844, Wilcoxon; Figure 6C).

Furthermore, the combined data from anesthetized mice (n = 348, six mice) showed similar deficits to that of the DR data (Figure S6D). Both qualitatively and quantitatively, the natural scene response eigenspectrum from anesthetized mice failed to flatten from τ1 (131ms) to τ2 (186 ms; Figures S6E and S6F). These deficits were also seen when analyzing individual animals (Figures 6A–6C), as measured by eigenspectrum slopes (−0.56 ± 0.03 at τ1 versus −0.55 ± 0.03 at τ2; p = 1.0, Wilcoxon; Figure 6A), the number of large PCs (11.3 ± 1.2 at τ1 and 10.2 ± 0.8 at τ2; p = 0.625, Wilcoxon; Figure 6B), and the percentage of total variance explained by PC1 (12.8% ± 1.4% at τ1 and 11.9% ± 0.6% at τ2; p = 0.438, Wilcoxon; Figure 6C).

Thus, irrespective of the quantitative method used, neither DR nor anesthetized mice showed a reduction of the redundancy in their natural scene responses akin to what was seen in awake normal reared mice. Importantly, at τ1 there were no significant differences between these groups in the eigenspectrum slope (H(2) = 0.833, p = 0.659, Kruskal-Wallis; Figures 4F and 6A), number of large PCs (H(2) = 0.663, p = 0.718, Kruskal-Wallis; Figures 4G and 6B), or percentage of total variance explained by PC1 (H(2) = 0.485, p = 0.785, Kruskal-Wallis; Figures 4H and 6C); illustrating that natural scene responses of these three groups of mice are initially similarly redundant. However, over time this redundancy is

significantly reduced only in awake normal reared mice with substantial coarse-to-fine SF processing and not in DR or anesthetized mice with significantly attenuated coarse-to-fine SF processing (Figures 6D–6F). Finally, these differences between awake, anesthetized, and dark-reared mice were not dependent upon the specific time points $\tau 2$ that we chose to analyze (Figures S6G–S6I).

DISCUSSION

In this study we find that a vast majority of V1 cells in adult mice have two temporally offset peaks in their STRFs. The two peaks lead to a rapid increase of the preferred SF, roughly tripling (1.64 octaves) over a brief response window. The coarse-to-fine processing of two-peak cells we reveal is uniquely different from what has been reported previously in anesthetized animals (Bredfeldt and Ringach, 2002; Vreysen et al., 2012), often consisting of large, abrupt rather than smooth, subtle shifts toward higher SFs. In other words, coarse-to-fine SF processing is dependent on the animal's awake or anesthetized state. Additionally, we show that it develops postnatally via visual experience and, most importantly, acts to dynamically shift the population SF tuning curve away from a low-pass representation. Strikingly, we illustrate that coarse-to-fine processing occurs when viewing ethologically relevant natural scenes and acts to drive a significant decrease in redundancy within V1's representation by shifting population responses away from the high-power, low-SF statistical regularities in natural scenes. Collectively, these findings reveal a computational role for coarse-to-fine processing in efficiently representing the spatial statistics of the complex stimuli that the visual system evolved and developed to encode and demonstrate that efficient coding operates on a previously unrealized timescale.

Temporal dynamics of natural scene responses

Our results highlight that V1's representation of natural scenes is not static, but rather evolves dynamically over time. Initially, the response is dominated by the low-SF components in the natural scenes, generating a population representation that is low dimensional and redundant. Over the response period, the cortical population rapidly shifts its SF tuning away from the low SF statistical regularities in the natural scenes, due largely (but not exclusively) to the temporal dynamics of two-peak cells. Subsequently, the population response becomes highly dimensional and efficient. This finding raises an interesting question regarding why V1 representations are not efficient to begin with. It is conceivable that V1's initial representation may be primarily driven by subcortical inputs, whose SF tuning largely match the SF statistics of the natural world (Grubb and Thompson, 2003; Piscopo et al., 2013; Tschetter et al., 2018), prior to having been processed by cortical circuitry. In other words, the initially redundant representation may reflect the neural scaffolding upon which the mechanisms driving coarse-to-fine SF processing are built and provides little to no computational benefit. However, previous studies demonstrating that coarse-to-fine SF processing also occurs in the dorsal lateral geniculate nucleus (dLGN; Allen and Freeman, 2006; Cai et al., 1997) and superior colliculus (SC; Chen et al., 2018) suggest this is unlikely. Alternatively, the initially redundant response could in fact be beneficial. Indeed, redundant neural codes are known to provide unique computational advantages unavailable to efficient ones (Młynarski and Hermundstad, 2021; Stringer et al.,

2019), such as being resilient to noise and producing representations that are generalizable (Stringer et al., 2019). Thus, it is likely that the coarse-to-fine processing of natural scenes we report here balances the benefits and drawbacks of both encoding schemes, allowing V1's representation to be initially robust and generalizable and eventually efficient, maximizing the transmission of information and enabling complex features to be encoded by downstream networks (DiCarlo et al., 2012; Stringer et al., 2019).

Circuit and developmental mechanisms for coarse-to-fine processing

Given the computational benefits we show coarse-to-fine processing to have, one might ask what circuit mechanism underlies this coarse-to-fine processing. One possibility is an entirely feed-forward mechanism whereby coarse-to-fine processing is inherited directly from subcortical structures. While coarse-to-fine SF shifting has been reported in the dLGN of cats (Allen and Freeman, 2006; Cai et al., 1997) and the SC of non-human primates (Chen et al., 2018), it is not clear whether the two-peak cells we describe here are present in those datasets and whether cortical feedback drives the SF shift they report. Another possible feedforward mechanism could be the coordinated convergence of two pathways with differing latencies and spatial preferences. While the existence of the rodent correlate of the magno- and parvocellular pathways in primates (Y and X cells in carnivores, respectively) is still a matter of debate (Frazor et al., 2004; Gao et al., 2010; Grubb and Thompson, 2003), the convergence of these pathways could, in theory, generate STRFs similar to that of two-peak cells. Also of interest are potential differences between mice and highly visual animals in coarse-to-fine processing and the underlying circuit mechanisms.

Previous studies have suggested temporally delayed suppression that is tuned to low SFs may drive coarse-to-fine SF processing (Allen and Freeman, 2006; Bredfeldt and Ringach, 2002). Interestingly, we find a similar relationship between the presence of low-SF suppression and coarse-to-fine processing at the population level, as well as a lack of both in anesthetized preparations, providing more evidence suggesting that the two may be related. Both intracortical feedback (Bredfeldt and Ringach, 2002) and subcortical feedforward (Allen and Freeman, 2006) mechanisms have been proposed as sources of this suppression. Relevant to the former, Ayzenshtat et al. (2016) have demonstrated a role for vasoactive intestinal polypeptide (VIP) expressing cortical inhibitory neurons in controlling the SF preferences of putative excitatory neurons in mouse V1 (Ayzenshtat et al., 2016), although the study did not directly address the temporal dynamics of SF tuning. Thus, the coarse-to-fine SF processing we report here may involve cortical inhibitory circuits including VIP cells.

Additionally, the second, high-SF, peak could be due to feedback inputs from higher cortical areas. Consistent with this idea, human fMRI studies reported that low SFs produced an initial increase of activity in prefrontal and temporo-parietal areas, followed by enhanced responses to high SFs in V1 (Peyrin et al., 2010). In mice, it has been reported that certain higher visual areas are functionally specialized to process high SFs (Andermann et al., 2011; Marshel et al., 2011; Tohmi et al., 2021), supporting this hypothesis. Future studies will be needed to characterize coarse-to-fine SF processing in these higher visual areas and determine their impact on V1.

Importantly, developmental studies can also provide clues to the circuit mechanisms underlying coarse-to-fine SF processing. A number of studies have described the developmental trajectories of the mouse visual system, ranging from retinal ganglion cells to primary and higher visual areas in the cortex (Chen et al., 2014; Hoy and Niell, 2015; Kang et al., 2013; Ko et al., 2013; Kowalewski et al., 2021; Rochefort et al., 2011; Tschetter et al., 2018; Wang et al., 2013). Future experiments are needed to link these developmental processes to the temporally dynamic shift of V1 SF tuning, particularly the development of cortical inhibitory circuits and functional maturation of higher visual area. It is interesting to note that our results complement previous reports on the development of SF tuning in V1 (Hoy and Niell, 2015; Kowalewski et al., 2021; Nishio et al., 2021) and the development of its behavioral correlate, visual acuity (Kang et al., 2013; Prusky and Douglas, 2003; Stephany et al., 2018). In fact, the development of coarse-to-fine SF processing revealed in our study might underlie the development of high-acuity vision, as both have been shown to develop postnatally and require visual experience (Kang et al., 2013; Prusky and Douglas, 2003; Stephany et al., 2018). Thus, future research on the relationship between coarse-to-fine SF processing and high-acuity vision could aid our understanding of the neural underpinnings of behavioral acuity and potentially provide clinical applications for the temporally dynamic process we report here.

Finally, given that we find coarse-to-fine SF processing is state dependent, it is interesting to speculate if and to what degree animal behavior might contribute to this temporally dynamic processing. Indeed, it has been well established that a variety of behaviors (e.g., locomotion, arousal, and attention; Ayaz et al., 2013; Hembrook-Short et al., 2019; Niell and Stryker, 2010; Savier et al., 2019; Vinck et al., 2015) directly modulate to the processing of visual information. Future research will be required to directly assess the contributions of such behaviors to the findings we report here.

Limitations of the study

In this work we used trial-averaged responses to assess how coarse-to-fine processing of natural scenes affects the representational efficiency of the underlying neural code. However, the true neural code occurs on individual trials, so our trial-averaged analyses may miss subtleties of the neural code that can only be revealed through investigating population responses on a trial-to-trial basis. Because responses of the individual neurons that make up the neural code are noisy and sparse, it becomes difficult to analyze the temporal dynamics of neural responses for individual trials. The common way to overcome this limitation is to average the response of a neuron either over time (Kowalewski et al., 2021; Stringer et al., 2019) or over trials (Churchland and Shenoy, 2007; Churchland et al., 2012; and as we did here). More recently, modeling methods have been developed to overcome these same technical limitations by attempting to infer the temporal dynamics of neural responses given sparse and noisy inputs (Pandarinath et al., 2018). This modeling approach has successfully recapitulated known population temporal dynamics that were first discovered using trial-averaged responses, demonstrating both its practicality as well as validating the use of trial-averaged responses in that particular case. Future research using methods such as these will provide promising avenues for investigating the temporally dynamic processing of information.

STAR★METHODS

RESOURCE AVAILABILITY

Lead contact—Any further information and requests for resources and reagents should be directed to the lead contact, Jianhua Cang (cang@virginia.com).

Materials availability—This study did not generate any new unique reagents.

Data and code availability

- All data reported in this paper will be shared by the lead contact upon request.
- All custom written Matlab scripts used in the current study is available online (Github: https://github.com/RolfSkyberg/CellReports2022–CtF-Processing, also Zenodo: https://doi.org/10.5281/zenodo.6320882).
- Any additional information required to reanalyze the data reported in this paper is available from the lead contact upon request.

EXPERIMENTAL MODEL AND SUBJECT DETAILS

Wild-type C57BL/6 mice at two developmental ages (P17-18, P40-P90) and of either sex were used in the experiments. All normal-reared (NR) animals were raised on a 12-h light/dark cycle, with food and water available ad libitum. Dark-reared (DR) animals were raised on a 24-h dark cycle from conception until the day of recording, with food and water available ad libitum. All experimental procedures were approved by the University of Virginia Institutional Animal Care and Use Committee.

METHOD DETAILS

Physiological recordings from mouse visual cortex—We performed physiological recordings from both anesthetized and awake mice. For anesthetized recordings, we followed our published surgical procedures (Chen et al., 2021; Shi et al., 2017, 2018). Briefly, mice were anesthetized with an intraperitoneal injection of urethane (1.2-1.3 g/kg in 10% saline) and supplemented by chlorprothixene (10 mg/kg in 4mg/mL water). Atropine (0.3 mg/kg in 10% saline) and dexamethasone (2.0 mg/kg in 10% saline) were administered subcutaneously to reduce secretions and edema, respectively. The animals body temperature was monitored and maintained at 37°C via a rectal probe connected to a feedback heater control module (Frederick Haer Company). Artificial tears (Henry Schein Medical) were applied to the eyes for protection during surgery. Mice were placed on the stereotaxic instrument (Narishige), with lidocaine applied on the ear bars. The scalp was shaved and skin was removed to expose the skull. A titanium custom-made head plate was mounted on the top of the skull with Metabond (Parkell). A craniotomy (~2.0 × 2.0 mm^2) was performed above the left visual cortex (V1; ~2.75mm lateral for adult mice and ~2.5mm for P17-18, and ~0.5mm anterior from lambda; Hoy and Niell, 2015; Niell and Stryker, 2008, 2010). The animal was then transferred to the recording station, still on the heating pad, with the head plate clamped in for fixation. A thin layer of silicon oil was applied on both eyes to replace the artificial tears.

For awake recordings, a survival surgery was first performed to implant the head plate. This was done with isoflurane anesthesia (4% for induction, 2% for maintenance, in O_2, ~0.5 L/min, VetFlo, Kent Scientific), and followed by the above procedures. After surgery, mice were given a dose of carprofen (5mg/kg, Sub-Q) and placed in a heated chamber until ambulatory. They were then transferred back to their home cage and monitored daily for pain and wound health. Two days after the head plating, mice were habituated to head-fixation for another 3-4 days. Recordings were performed once they were comfortable with the setup. On the day of the recording a craniotomy was done under isoflurane anesthesia, at least 4 h before the recording. For DR mice, surgical procedures were done using red-shifted light and an eye cover to minimize ambient light exposure.

Recordings were done using high-density multielectrode silicon microprobes developed by Sotiris Masmanidis from the University of California, Los Angeles (Yang et al., 2020). We used the “128AxN Sharp”, “128M” and “128J” probe designs (Figure S1A). The probe was carefully inserted into the craniotomy and lowered to a depth of ~0.9mm below the cortical surface. After reaching its final depth, the probe was allowed to sit for ~15 min before recordings began.

Visual stimulation—Visual stimuli were generated with MATLAB Psychophysics toolbox (Brainard, 1997; Niell and Stryker, 2008) (RRID: CDR_002881) on an LCD monitor (52.7cm x 29.6cm, 60Hz refresh rate, ~50cd/m^2 mean luminance, gamma corrected). The monitor was placed 25cm away from the mouse. For each recording the monitor was slightly adjusted so that cells’ receptive fields were near the center of the monitor. Thus, the monitor center in visual space varied between roughly 0° and 20° across the azimuth (0° representing the center of the binocular visual field) and −10° and 10° in elevation (0° representing eye-level). Receptive fields were mapped using a white bar on a black background at the beginning of every recording.

Subspace-forward correlation: To measure and analyze the temporal dynamics of spatial frequency (SF) tuning we used subspace forward-correlation to measure the spatiotemporal receptive field of V1 neurons. This technique is mathematically identical to the subspace reverse-correlation method described by (Bredfeldt and Ringach, 2002; Frazor et al., 2004; Vreysen et al., 2012). Briefly, we recorded neural responses to a rapid sequence of sinusoidal gratings of varying orientations (0°, 45°, 90°, 135°), spatial phases (0, $\pi/2$, π, $3\pi/2$ rad), and SFs (0.02, 0.04, 0.08, 0.1, 0.12, 0.16, 0.2, 0.24, 0.28, 0.32 c/d; Figure 1A). We included spatial phase and orientation as variables to cover the subspace of the majority of V1 neurons’ receptive fields. Blank images of uniform luminance were interleaved into the sequence to provide a measure of the baseline firing (Figure 1A). The probability of a blank image being presented was equal to that of showing any one SF, irrespective of phase and orientation. Our stimulus set consisted of 176 conditions (10 SFs x 4 orientations x 4 spatial phase +16 blanks) that were shown to the animal in a randomized order at 60Hz and repeated 800 times for a total recording time of ~39 min. Images were presented in 60° circular window centered approximately on the cells’ receptive fields. In a subset of animals that were shown both natural scenes and gratings, we used a smaller number of repeats (400) to keep total recording times practical.

Natural scenes: Animals were shown a collection of 150 natural scenes, acquired from a previously published natural scene database (http://doi.org/10.25378/janelia.6845348.v4; Stringer et al., 2019). These images were manually selected by Stringer et al. (2019) to ensure that they contained a mixture of low and high spatial frequencies and were uniformly contrast normalized. We randomly selected 150 of these contrast-normalized naturalistic scenes from the 2800 image database. Each image was presented in a 60° circular window, centered approximately on the cells' receptive fields for 300ms. Blank images of uniform luminance were interleaved between each naturalistic scene for 200ms before subsequent stimuli were presented. Each naturalistic scene was shown 20 times in a pseudorandomized order for a total recording time of ~25 min.

Filtered natural scenes: A subset of 60 of the above natural scenes were filtered, using the image processing toolbox on MATLAB (Mathworks Inc, Sherborm MA; RRID: SCR_001622), to generate variants of natural scenes with altered SF statistics (Figures 3A and 3B). To do this, we filtered the natural scenes with a Gaussian filter with a standard deviation of 2. The resulting low-pass filtered scenes had significantly attenuated SFs above ~0.08 c/d (Figures 3A and 3B). By subtracting the low-pass filtered scenes from their unfiltered originals we generated the high-pass variants of the natural scenes. These high-pass filtered scenes had significantly attenuated SFs below ~0.08 c/d. Following filtering, all scenes were contrast normalized so that the average stimulus luminance did not differ across scenes. During recordings, all 180 natural scenes (60 scenes x 3 variants) were presented in a 60° circular window, centered approximately on the cells' receptive fields for 300ms. Blank images of uniform luminance were interleaved between each naturalistic scene for 200ms before subsequent stimuli were presented. Each naturalistic scene was shown 30 times in a pseudorandomized order for a total recording time of ~45 min.

Data analysis—Voltage signals from the probes were band-pass filtered (300-6000Hz) and recorded at 20 kHz sampling rate (RHD Evaluation System, Intan Technologies, RRID:SCR_019278). Spike waveforms were sorted offline using the software package MountainSort (Chung et al., 2017; RRID:SCR_017446). We separated spike clusters into single-units versus multi-units based on two clustering metrics. One was noise overlap, which measures how much overlap the cluster has to a cluster comprised of randomly sampled spikes from noise. The second was isolation, which indicates how well isolated a cluster is from other clusters. The clusters that have a noise overlap <0.08 and an isolation of >0.96 were classified into single units (Figure S1B; Chen et al., 2021). By plotting the variance of a single unit's responses to all grating stimuli, we determined if the single unit was responsive or not. Single units were considered responsive, and included in subsequent analyses, if their variance plot generated a peak between 30 and 180ms. When recording natural scene responses, we used a more objective selection criterion and included any single unit that responded to at least 1 of the natural images by firing at least 1 spike.

Subspace-forward correlation: Each grating stimulus was generated with specific values of orientation θ, SF f, and phase φ. For simplicity, we represent the 3-parameter combination with an array θ. We triggered the spike train of a neuron at the time at which a specific grating was presented and calculated the probability that a cell generated a spike at every

time bin τ following the stimulus onset Pr(θ, τ), with 1ms bin width, up to 200ms after the stimulus onset. A similar spike histogram was calculated, with the trigger time as the onset of a blank image. This spike histogram provided the baseline B(τ). The relative strength of the response was given by R(θ, τ) = Pr(θ,τ) - B(τ) Figure 1A), A R(θ,τ) value of zero indicate the cell's response to a grating stimulus was equal to that of the blank stimulus. Positive and negative values of R(θ,τ) indicate excitation and suppression, respectively. We show that using blank subtracted values did not lead to erroneous or systematic confounds in our assessment of coarse-to-fine processing across animal groups (Figure S7). For both short (τ < 30ms) and long (τ > 180ms) time lags, R(θ,τ) is expected to be flat and near zero, indicating no causal relationship between the stimulus and the response. To reduce the noise in the estimation, we filtered R(θ,τ) with a 16.6ms wide square wave window. Finally, the values of R(θ,τ) were converted to firing rate (spikes/s) by dividing by the bin width 0.001 (s).

Although the grating stimuli were characterized by 3 parameters (orientation, SF, and phase), we put the focus of our analysis on SF. We marginalized R(θ,τ) with respect to the orientation and phase parameters with the following procedure. For each combination of orientation and SF, we first picked the phase that evoked the strongest response, and discarded all R(θ,τ) that were associated with other phase values. The number of parameter combinations comprising R(θ,τ) was reduced from 160 to 40. We then averaged R(θ,τ) over orientation. The resulting R(θ,τ) was a 2D function of SF and time, which we will henceforth denote as R(f,τ). Due to the 10 discrete values of SF used in the experiment, the data of R(f,τ) was a matrix R with 10 rows. The columns of R represented a cell's SF tuning over time. Using this response matrix R we first quantified a cell's time-integrated SF tuning curve (i.e., without considering how it changes over time). To do this, we summed all values of R(f,τ) that were greater than a threshold value (2.5 s.d. above the average R(f,τ) between τ = 0 and τ = 30).

To measure if and how a cell's SF tuning changed over time we first calculated the time point τ that evoked the strongest response in each cell. We defined this time point and the SF preference of the cell at this time point as T_{pk1} and f_{pk1}, respectively. Many cells in our data set showed a temporally delayed second peak in R(f,τ) Figure 1C). We defined the time point and preferred spatial frequency of the cell at this time point as τ_{pk2} and f_{pk2}, respectively. To quantitatively determine if a cell had a temporally delayed second peak we developed a template matching algorithm which compared the SF responses R(f,τ), to R(f_{pk1},τ). This template matching algorithm separated each R(f,τ) into a fitted curve matrix and residual curve matrix based on R(f_{pk1},τ). We then calculated the τ in which the strongest response occurred for both the fit and residual curve matrix (defined as τ_{fit} and τ_{res}, respectively). By definition $\tau_{fit} = \tau_{pk1}$ and $\tau_{res} \neq \tau_{pk1}$. τ_{res} occurred at some τ after τ_{pk1}. If any response R(f,τ_{res}) was greater than a threshold of 2.5 s.d. above the average R(f,τ) between τ = 0 and τ = 30, we considered that cell to have a temporally delayed second peak at τ_{res}. In these cells we set τ_{pk2} equal to τ_{res} and f_{pk2} equal to the preferred SF at τ_{pk2}. Cells that did not pass this criterion were considered to not have a temporally delayed second peak in R(f,τ) and were not given values for τ_{pk2} or f_{pk2} (Figure 1B). The cells with and without a temporally delayed second peak in R(f,τ) were referred to as "2 peak cells" and "1 peak cells", respectively (for examples see Figures 1B and 1C).

To determine how the preferred SF of 2 peak cells changed during their response, we compared f_{pk1} and f_{pk2}: $\Delta f_{pk} = \log_2(f_{pk2}/f_{pk1})$. This value estimates Δf_{pk} in octaves. Because 1 peak cells do not have a value for f_{pk2} we gave them a $\Delta f_{pk} = 0$. Note that this method for determining Δf_{pk} is similar but not identical to what has been previously published (Bredfeldt and Ringach, 2002; Vreysen et al., 2012).

Natural scenes: For each of the contrast-normalized natural scenes, we generated peri-stimulus time histograms (PSTHs), which represent the average response of a cell to all repeats of the scene. Each PSTH was filtered with a 16.6ms square wave window and divided by the width of the time bin. Using these PSTHs we created a natural scene response matrix N, in which the *i*-th row corresponds to the *i*-th natural scene of the stimulus set and the *j*-th column corresponds to the *j*-th time bin. By averaging across the rows of N, we calculate the cell's mean PSTH across all scenes. To prevent future analyses from being dominated by a few neurons with high firing rates, we normalized the firing rate of each neuron to the maximum value across all the elements of N; this is particularly important with PCA-based analyses (Churchland et al., 2012; Kaufman et al., 2016; Yu et al., 2009).

Measuring neural population response structure over time: To measure how the neural population response structure evolves over time we used Principal Component Analysis (PCA) to reduce the dimensionality of the neural response dataset at each time point τ independently. Each dataset contained the response of n neurons to 150 natural scenes. The response to one scene at any time point τ can be represented as a single point in an n-dimensional space. We call the subspace occupied by all 150 points at any τ the neural response manifold. Through PCA we assessed the dimensionality of this neural response manifold separately at each τ by measuring the number of principal components (PCs) needed to describe the signal within it. To be clear, PCA was recomputed at each τ. A majority of the "signal" in datasets is captured by the larger PCs, while smaller PCs represent "noise" (Farmer, 1971; Lehky et al., 2014). Thus, measuring the dimensionality of the "signal" in a dataset becomes a matter of counting the number of large PCs.

We used three measures to quantify and compare changes in dimensionality of a neural response manifold over time. First, we rank-ordered the PCs as a function of the amount of variance they describe (i.e. eigenspectrum). We then randomly shuffled our dataset and generated an eigenspectrum for the shuffled dataset. To shuffle the data, we reorganized the response matrix N into a 1D array, randomly permutated those elements in the 1D array, and then reshaped the array back into the original matrix N size. Randomly shuffling the data destroys the structure of the original response signal while maintaining the same total variance in the dataset. Therefore, by comparing the eigenspectra generated by the shuffled and original dataset we can assess which PCs correspond to the signal structure and which correspond to noise. PCs from the original dataset that were larger than their shuffled counterparts were considered to correspond to signal in the data (i.e. large), while the rest were considered to correspond to noise (i.e. small). This can be graphically represented as the point at which the original and shuffled eigenspectra intersect (Figure 4D, inset). Thus, by measuring the number of large PCs we can assess the dimensionality of a neural response manifold at any τ. This shuffling method has been used by previously published

studies to assess dimensionality (Horn, 1965; Lehky et al., 2014; Peres-Neto et al., 2005). To determine if and how the dimensionality of a neural response manifold changed throughout the response period we calculated the change in the number of large PCs between two time points: $\Delta\text{LargePCs} = \tau2_{\text{LargePCs}} = \tau1_{\text{LargePCs}}$. Positive and negative values of ΔLargePCs indicate increases and decreases in the dimensionality of the neural response manifold over the response period, respectively.

Second, we calculated the slope of the eigenspectrum at any τ. Because high-dimensional neural response manifolds will share the variance associated with the "signal" across more PCs than low-dimensional ones, the eigenspectrum they generate will be flatter (Figure 4A; Stringer et al., 2019). Thus, the slope of the eigenspectrum is indicative of the dimensionality: the steeper the slope the lower the dimensionality of the underlying response manifold. To calculate the eigenspectrum slope we computed a linear fit of the first 20 (for pooled data) or 10 (for individual animals) PCs in log-log space. This was a judicious choice based on two observations. 1) These values roughly corresponded to the number of large PCs we discovered using our shuffling method (described above). 2) Using more PCs significantly attenuated how well the curve fit the eigenspectrum due to many small PCs not describing much of the variance. We measured the change in the eigenspectrum slope from $\tau1$ to $\tau2$ as: $\Delta\text{Slope} = \tau2_{\text{Slope}} = \tau1_{\text{Slope}}$. Positive and negative values of ΔSlope indicate increasing and decreasing dimensionality of the neural response manifold over the response period, respectively.

Third, we calculated the change in the percentage of the total variance described the first PC between $\tau1$ and $\tau2$ as: $\Delta\text{Percent} = \tau2_{\text{Percent}} - \tau1_{\text{Percent}}$. We chose to limit this analysis to PC1 for two reasons. 1) PC1 by definition describes the largest amount of variance within a neural response manifold at any given τ. 2) We noticed that PC1 was the most variable over the response period (see Figures 3F or 4C). Unlike the previous two measures, positive values of ΔPercent indicate decreases in the dimensionality while negative values indicate increases.

To determine how the dimensionality of a neural response manifold changed over the response period we compared these three measures at the two time points, $\tau1$ and $\tau2$. One could choose any two time points in which there is a sufficiently strong population response. However, because we were interested in how the dimensionality of a neural response manifold might be shaped by the coarse-to-fine SF processing we described in the cortex, we chose time points based on our findings from our recordings using filtered natural scenes. We chose to use the temporal windows of 100–150ms and 1251–225ms to define $\tau1$ and $\tau2$, respectively.

These temporal windows were chosen because 150ms provided relatively good separation between the average high-pass filtered and low-pass filtered or unfiltered natural scene peak response times (Figures 3G–3H and S3E–S3G). The time points within each temporal window where PC1 reached its local maximum value were used as $\tau1$ and $\tau2$. However, additional analyses were done to demonstrate that the specific $\tau2$ we chosen did not erroneously affect our results (Figures S6G–S6I). In fact, our method for selecting $\tau2$ often

resulted in slightly more conservative estimates of changes in efficiency than if we were to use an earlier or later time point.

Measuring natural scene response variability: We measured the variability of the responses to natural scenes using Fano factor, the ratio between the variance of the spike count over the mean of the spike count[31]. Responses of individual trials were each filtered with a 16.6ms wide square wave window. At each time point, we computed the variance of the spike count and the mean of the spike count for each natural scene. We repeated this calculation for all the natural scenes and all the neurons. Thus, a neuron's response to one natural scene at any given time, τ, was represented by two numbers: the variance and mean of the spike count. At every τ we obtained the linear regression (model II) of the variance versus the mean (Figure S3). We used model II regression because variance and mean are both dependent variables. The slope of the regression line was our estimate of the Fano factor (Figure S3).

Relating dimensionality of a neural response to efficiency of a neural representation: Notably, the dimensionality of a neural response manifold is directly related to the amount of redundancy in the neural responses that make up the manifold. In an extremely redundant representation where all neurons responded identically, the dimensionality of the neural response manifold will be low (equal to 1) and the number of PCs required to capture the variance in this neural response manifold will also be low (equal to 1). On the other extreme, if all n neurons generated distinctly unique responses (i.e., no redundancy), the dimensionality of their neural response manifold would be high (equal to n). In this case, the number of PCs required to capture all the variance in the response manifold would also be high (equal to n). In reality neural codes fall somewhere between these two extremes, as neural responses are often somewhat redundant but never completely so. However, these hypothetical extremes help to generate intuition as to how we can assess the efficiency of a neural response by measuring the dimensionality of the neural response manifold it creates. For a graphical representation of this concept, where $n = 2$ and the number of natural images = 5, see Figure 4A.

QUANTIFICATION AND STATISTICAL ANALYSIS

All pooled data were presented as means ± SEM unless otherwise stated. The Mann-Whitney test was applied for comparing data from different groups of cells, while the Wilcoxon signed-rank test was applied for paired comparisons. Two-sided statistical tests were used. The Kruskal-Wallis test was used to compare data from three groups of cells. All analyses and graph plotting were performed in MATLAB (Mathworks Inc, Sherborm MA; RRID:SCR_001622). The number of cells and animals, as well as details of statistical tests, are provided in Results. In figures, *$p < 0.05$, **$p < 0.01$ and ***$p < 0.001$. No statistical methods were used to predetermine sample sizes, but our sample sizes are similar to those reported in the field. We did not randomly assign animals to groups as it is not applicable to the experimental design of this study.

Supplementary Material

Refer to Web version on PubMed Central for supplementary material.

ACKNOWLEDGMENTS

We thank Dr. Ali Güler, Dr. Adema Ribic, and Qijun Tang for help with dark rearing; Dr. Dan Meliza and members of the Cang lab for discussion and comments on the manuscript; and the Jefferson Scholars Foundation for financial support. This work was supported by US National Institutes of Health (NIH) grants R01EY026286 and R01EY020950 to J.C and F32EY032360 to R.S.

REFERENCES

Allen EA, and Freeman RD (2006). Dynamic spatial processing originates in early visual pathways. J. Neurosci 26, 11763–11774. [PubMed: 17093097]

Andermann ML, Kerlin AM, Roumis DK, Glickfeld LL, and Reid RC (2011). Functional specialization of mouse higher visual cortical areas. Neuron 72, 1025–1039. [PubMed: 22196337]

Atick JJ, and Redlich AN (1990). Towards a theory of early visual processing. Neural Comput 2, 308–320.

Attneave F (1954). Some informational aspects of visual perception. Psychol. Rev 61, 183–193. [PubMed: 13167245]

Ayaz A, Saleem AB, Schölvinck ML, and Carandini M (2013). Locomotion controls spatial integration in mouse visual cortex. Curr. Biol 23,890–894. [PubMed: 23664971]

Ayzenshtat I, Karnani MM, Jackson J, and Yuste R (2016). Cortical control of spatial resolution by VIP $^{+}$ interneurons. J. Neurosci 36, 11498–11509. [PubMed: 27911754]

Barlow HB (1961). In Sensory Communication (MIT Press), pp. 217–234.

Brainard DH. (1997). The Psychophysics toolbox. Spat. Vis 10, 433–436. [PubMed: 9176952]

Bredfeldt CE, and Ringach DL (2002). Dynamics of spatial frequency tuning in macaque V1. J. Neurosci 22, 1976–1984. [PubMed: 11880528]

Cai D, Deangelis GC, and Freeman RD (1997). Spatiotemporal receptive field organization in the lateral geniculate nucleus of cats and kittens. J. Neurophysiol 78, 1045–1061. [PubMed: 9307134]

Chen C-Y, Sonnenberg L, Weller S, Witschel T, and Hafed ZM (2018). Spatial frequency sensitivity in macaque midbrain. Nat. Commun 9, 2852. [PubMed: 30030440]

Chen H, Liu X, and Tian N (2014). Subtype-dependent postnatal development of direction- and orientation-selective retinal ganglion cells in mice. J. Neurophysiol 112, 2092–2101. [PubMed: 25098962]

Chen H, Savier EL, DePiero VJ, and Cang J (2021). Lack of evidence for stereotypical direction columns in the mouse superior colliculus. J. Neurosci 41, 461–473. [PubMed: 33214319]

Chung JE, Magland JF, Barnett AH, Tolosa VM, Tooker AC, Lee KY, Shah KG, Felix SH, Frank LM, and Greengard LF (2017). A fully automated approach to spike sorting. Neuron 95, 1381–1394.e6. [PubMed: 28910621]

Churchland MM, and Shenoy KV (2007). Temporal complexity and heterogeneity of single-neuron activity in premotor and motor cortex. J. Neurophysiol 97, 4235–4257. [PubMed: 17376854]

Churchland MM, Yu BM, Cunningham JP, Sugrue LP, Cohen MR, Corrado GS, Newsome WT, Clark AM, Hosseini P, Scott BB, et al. (2010). Stimulus onset quenches neural variability: a widespread cortical phenomenon. Nat. Neurosci 13, 369–378. [PubMed: 20173745]

Churchland MM, Cunningham JP, Kaufman MT, Foster JD, Nuyujukian P, Ryu SI, and Shenoy KV (2012). Neural population dynamics during reaching. Nature 487, 51–56. [PubMed: 22722855]

Dan Y, Atick JJ, and Reid RC (1996). Efficient coding of natural scenes in the lateral geniculate nucleus: experimental test of a computational theory. J. Neurosci 16, 3351–3362. [PubMed: 8627371]

DiCarlo JJ, Zoccolan D, and Rust NC (2012). How does the brain solve visual object recognition? Neuron 73, 415–434. [PubMed: 22325196]

Farmer SA (1971). An investigation into the results of principal component analysis of data derived from random numbers. The Statistician 20, 63.

Frazor RA, Albrecht DG, Geisler WS, and Crane AM (2004). Visual cortex neurons of monkeys and cats: temporal dynamics ofthe spatial frequency response function. J. Neurophysiol 91, 2607–2627. [PubMed: 14960559]

Gao E, DeAngelis GC, and Burkhalter A (2010). Parallel input channels to mouse primary visual cortex. J. Neurosci 30, 5912–5926. [PubMed: 20427651]

Gjorgjieva J, Sompolinsky H, and Meister M (2014). Benefits of pathway splitting in sensory coding. J. Neurosci 34, 12127–12144. [PubMed: 25186757]

Grubb MS, and Thompson ID (2003). Quantitative characterization of visual response properties in the mouse dorsal lateral geniculate nucleus. J. Neurophysiol 90, 3594–3607. [PubMed: 12944530]

Hembrook-Short JR, Mock VL, Usrey WM, and Briggs F (2019). Attention enhances the efficacy of communication in V1 local circuits. J. Neurosci 39, 1066–1076. [PubMed: 30541911]

Horn JL (1965). A rationale and test for the number of factors in factor analysis. Psychometrika 30, 179–185. [PubMed: 14306381]

Hoy JL, and Niell CM (2015). Layer-specific refinement of visual cortex function after eye opening in the awake mouse. J. Neurosci 35, 3370–3383. [PubMed: 25716837]

Kang E, Durand S, LeBlanc JJ, Hensch TK, Chen C, and Fagiolini M (2013). Visual acuity development and plasticity in the absence of sensory experience. J. Neurosci 33, 17789–17796. [PubMed: 24198369]

Karklin Y, and Lewicki MS (2009). Emergence of complex cell properties by learning to generalize in natural scenes. Nature 457, 83–86. [PubMed: 19020501]

Karklin Y, and Simoncelli EP (2011). Efficient coding of natural images with a population of noisy Linear-Nonlinear neurons. Adv. Neural Inf. Process. Syst 24, 999–1007. [PubMed: 26273180]

Kaufman MT, Seely JS, Sussillo D, Ryu SI, Shenoy KV, and Churchland MM (2016). The largest response component in the motor cortex reflects movement timing but not movement type. Eneuro 3, ENEURO.0085-116.2016.

Ko H, Cossell L, Baragli C, Antolik J, Clopath C, Hofer SB, and Mrsic-Flogel TD (2013). The emergence of functional microcircuits in visual cortex. Nature 496, 96–100. [PubMed: 23552948]

Kowalewski NN, Kauttonen J, Stan PL, Jeon BB, Fuchs T, Chase SM, Lee TS, and Kuhlman SJ (2021). Development of natural scene representation in primary visual cortex requires early postnatal experience. Curr. Biol 31, 369–380.e5. [PubMed: 33220181]

Lehky SR, Kiani R, Esteky H, and Tanaka K (2014). Dimensionality of object representations in monkey inferotemporal cortex. Neural Comput. 26, 2135–2162. [PubMed: 25058707]

Marshel JH, Garrett ME, Nauhaus I, and Callaway EM (2011). Functional specialization of seven mouse visual cortical areas. Neuron 72, 1040–1054. [PubMed: 22196338]

Matsumoto N, Okada M, Sugase-Miyamoto Y, Yamane S, and Kawano K (2005). Population dynamics of face-responsive neurons in the inferior temporal cortex. Cereb. Cortex 15, 1103–1112. [PubMed: 15563724]

Mazer JA, Vinje WE, McDermott J, Schiller PH, and Gallant JL (2002). Spatial frequency and orientation tuning dynamics in area V1. Proc. Natl. Acad. Sci 99, 1645–1650. [PubMed: 11818532]

Menz MD, and Freeman RD (2003). Stereoscopic depth processing in the visual cortex: a coarse-to-fine mechanism. Nat. Neurosci 6, 59–65. [PubMed: 12469131]

Młynarski WF, and Hermundstad AM (2021). Efficient and adaptive sensory codes. Nat. Neurosci 24, 998–1009. [PubMed: 34017131]

Niell CM, and Stryker MP (2008). Highly selective receptive fields in mouse visual cortex. J. Neurosci 28, 7520–7536. [PubMed: 18650330]

Niell CM, and Stryker MP (2010). Modulation of visual responses by behavioral state in mouse visual cortex. Neuron 65, 472–479. [PubMed: 20188652]

Nirenberg S, Carcieri SM, Jacobs AL, and Latham PE (2001). Retinal ganglion cells act largely as independent encoders. Nature 411, 698–701. [PubMed: 11395773]

Nishio N, Hayashi K, Ishikawa AW, and Yoshimura Y (2021). The role of early visual experience in the development of spatial-frequency preference in the primary visual cortex. J. Physiol 599, 1–22.

Olshausen BA, and Field DJ (1996a). Emergence of simple-cell receptive field properties by learning a sparse code for natural images. Nature 381, 607–609. [PubMed: 8637596]

Olshausen BA, and Field DJ (1996b). Natural image statistics and efficient coding. Netw. Comput. Neural Syst 7, 333–339.

Pandarinath C, O'Shea DJ, Collins J, Jozefowicz R, Stavisky SD, Kao JC, Trautmann EM, Kaufman MT, Ryu SI, Hochberg LR, Henderson JM, Shenoy KV, Abbott LF, and Sussillo D (2018). Inferring single-trial neural population dynamics using sequential auto-encoders. Nature Methods 15, 805–815. [PubMed: 30224673]

Peres-Neto PR, Jackson DA, and Somers KM (2005). How many principal components? stopping rules for determining the number of non-trivial axes revisited. Comput. Stat. Data Anal 49, 974–997.

Perge JA, Borghuis BG, Bours RJE, Lankheet MJM, and van Wezel RJA (2005). Temporal dynamics of direction tuning in motion-sensitive macaque area MT. J. Neurophysiol 93, 2104–2116. [PubMed: 15537817]

Peyrin C, Michel CM, Schwartz S, Thut G, Seghier M, Landis T, Marendaz C, and Vuilleumier P (2010). The neural substrates and timing of top-down processes during coarse-to-fine categorization of visual scenes: a combined fMRI and ERP study. J. Cogn. Neurosci 22, 2768–2780. [PubMed: 20044901]

Piscopo DM, El-Danaf RN, Huberman AD, and Niell CM (2013). Diverse visual features encoded in mouse lateral geniculate nucleus. J. Neurosci 33, 4642–4656. [PubMed: 23486939]

Pitkow X, and Meister M (2012). Decorrelation and efficient coding by retinal ganglion cells. Nat. Neurosci 15, 628–635. [PubMed: 22406548]

Prusky GT, and Douglas RM (2003). Developmental plasticity of mouse visual acuity: plasticity of visual acuity in mice. Eur. J. Neurosci 17, 167–173. [PubMed: 12534981]

Ratliff CP, Borghuis BG, Kao Y-H, Sterling P, and Balasubramanian V (2010). Retina is structured to process an excess of darkness in natural scenes. Proc. Natl. Acad. Sci 107, 17368–17373. [PubMed: 20855627]

Ringach DL, Hawken MJ, and Shapley R (1997). Dynamics of orientation tuning in macaque primary visual cortex. Nature 387, 281–284. [PubMed: 9153392]

Rochefort NL, Narushima M, Grienberger C, Marandi N, Hill DN, and Konnerth A (2011). Development of direction selectivity in mouse cortical neurons. Neuron 71, 425–432. [PubMed: 21835340]

Roy S, Jun NY, Davis EL, Pearson J, and Field GD (2021). Inter-mosaic coordination of retinal receptive fields. Nature 592, 409–413. [PubMed: 33692544]

Ruderman DL, and Bialek W (1994). Statistics of natural images: scaling in the woods. Phys. Rev. Lett 73, 814–817. [PubMed: 10057546]

Savier EL, Chen H, and Cang J (2019). Effects of locomotion on visual responses in the mouse superior colliculus. J. Neurosci 39, 9360–9368. [PubMed: 31570535]

Shi X, Barchini J, Ledesma HA, Koren D, Jin Y, Liu X, Wei W, and Cang J (2017). Retinal origin of direction selectivity in the superior colliculus. Nat. Neurosci 20, 550–558. [PubMed: 28192394]

Shi X, Jin Y, and Cang J (2018). Transformation of feature selectivity from membrane potential to spikes in the mouse superior colliculus. Front. Cell. Neurosci 12, 163. [PubMed: 29970991]

Simoncelli EP, and Olshausen BA (2001). Natural image statistics and neural representation. Annu. Rev. Neurosci 24, 1193–1216. [PubMed: 11520932]

Stephany C-É, Ma X, Dorton HM, Wu J, Solomon AM, Frantz MG, Qiu S, and McGee AW (2018). Distinct circuits for recovery of eye dominance and acuity in murine amblyopia. Curr. Biol 28, 1914–1923.e5. [PubMed: 29887305]

Stringer C, Pachitariu M, Steinmetz N, Carandini M, and Harris KD (2019). High-dimensional geometry of population responses in visual cortex. Nature 571, 361–365. [PubMed: 31243367]

Sugase Y, Yamane S, Ueno S, and Kawano K (1999). Global and fine information coded by single neurons in the temporal visual cortex. Nature 400, 869–873. [PubMed: 10476965]

Tohmi M, Tanabe S, and Cang J (2021). Motion streak neurons in the mouse visual cortex. Cell Rep. 34, 108617. [PubMed: 33440151]

Tschetter WW, Govindaiah G, Etherington IM, Guido W, and Niell CM (2018). Refinement of spatial receptive fields in the developing mouse lateral geniculate nucleus is coordinated with excitatory and inhibitory remodeling. J. Neurosci 38, 4531–4542. [PubMed: 29661964]

Vinck M, Batista-Brito R, Knoblich U, and Cardin JA (2015). Arousal and locomotion make distinct contributions to cortical activity patterns and visual encoding. Neuron 86, 740–754. [PubMed: 25892300]

Vinje WE, and Gallant JL (2000). Sparse coding and decorrelation in primary visual cortex during natural vision. Science 287, 1273–1276. [PubMed: 10678835]

Vreysen S, Zhang B, Chino YM, Arckens L, and Van den Bergh G (2012). Dynamics of spatial frequency tuning in mouse visual cortex. J. Neurophysiol 107, 2937–2949. [PubMed: 22402662]

Wang B-S, Feng L, Liu M, Liu X, and Cang J (2013). Environmental enrichment rescues binocular matching of orientation preference in mice that have a precocious critical period. Neuron 80, 198–209. [PubMed: 24012279]

Yang L, Lee K, Villagracia J, and Masmanidis SC (2020). Open source silicon microprobes for high throughput neural recording. J. Neural Eng 17, 016036. [PubMed: 31731284]

Yu BM, Cunningham JP, Santhanam G, Ryu SI, Shenoy KV, and Sahani M (2009). Gaussian-process factor Analysis for low-dimensional single-trial analysis of neural population activity. J. Neurophysiol 102, 614–635. [PubMed: 19357332]

Highlights

- Majority of V1 neurons in awake mice have coarse-to-fine receptive field dynamics
- Mice process complex natural scenes in a coarse-to-fine manner
- Coarse-to-fine processing drives efficient coding of natural scenes in awake mice
- Coarse-to-fine processing develops via visual experience and requires wakefulness

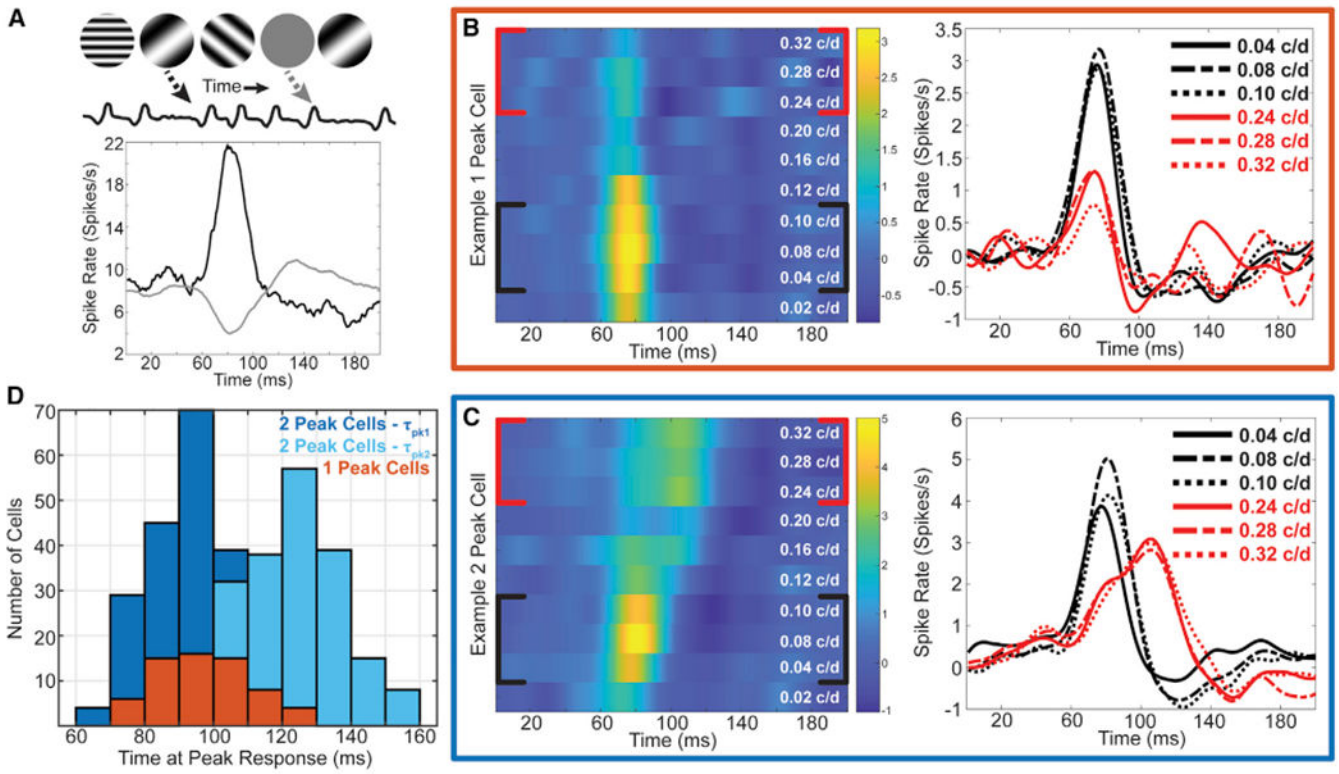

Figure 1. Mapping spatiotemporal receptive fields of mouse V1 cells

(A) Diagram of the subspace forward correlation method. Top, the stimulus is a rapid sequence of sinusoidal gratings of varying spatial frequencies (SF), orientations, and phases. Each neuron's spike responses following the onset of all repeats of a given stimuli (black) or blanks (gray) are binned and summed into individual peri-stimulus time histograms (PSTHs). Bottom, example PSTHs to a particular stimulus (black) and blank (gray).

(B) Representative one-peak cell from V1 of an awake mouse. Left, heatmap of responses to each SF. Black and red brackets indicate corresponding responses plotted to the right. Scale bar denotes firing rate in spikes/s. Right, low-SF (black) and high-SF (red) responses of the same cell. c/d, cycles/degree.

(C) Same as (B) but for a representative two-peak cell.

(D) Distribution of latencies to peak response for cells from awake mice. Orange, one-peak cells; dark blue, two-peak cells first peak (τ_{pk1}); light blue, two-peak cells second peak (τ_{pk2}). See also Figure S7.

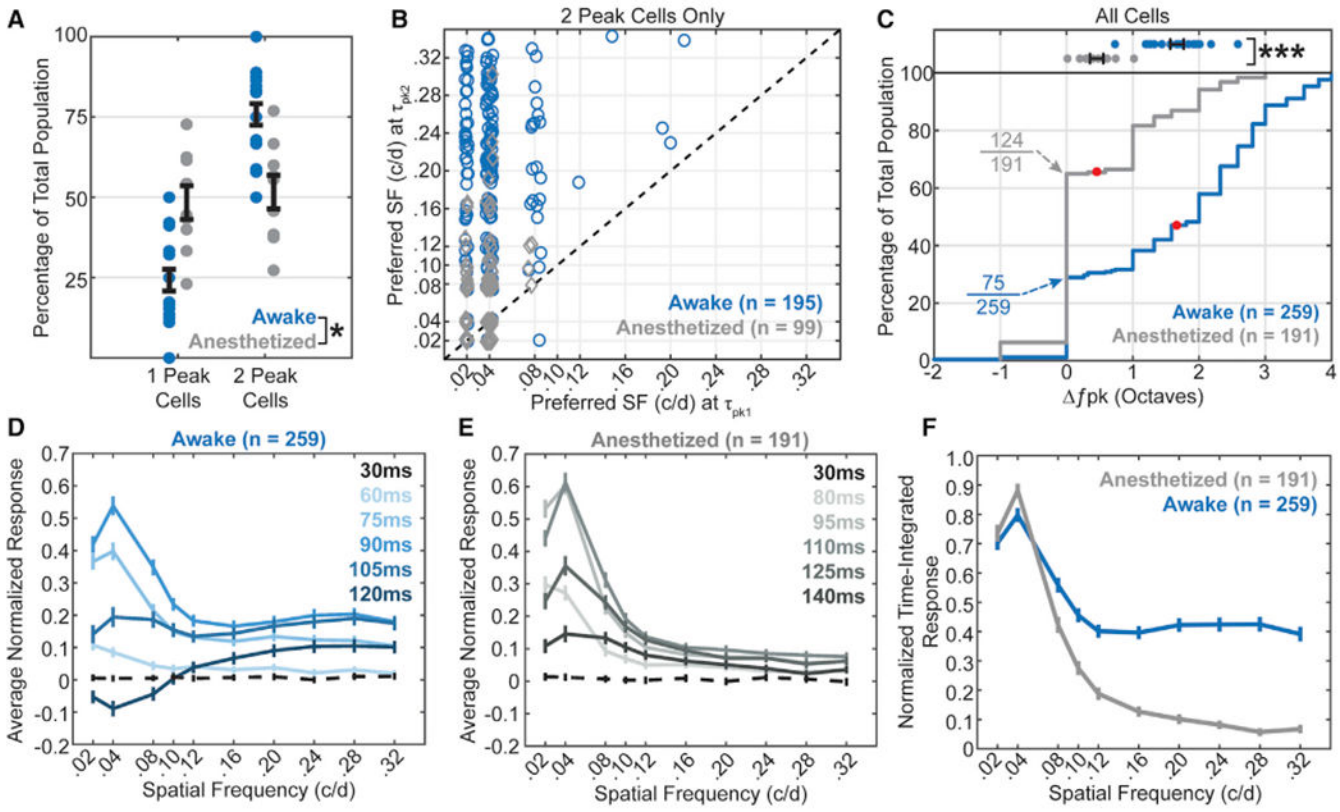

Figure 2. State-dependent coarse-to-fine SF processing in mouse V1

(A) Proportion of one- and two-peak cells from V1 of awake (blue) and anesthetized (gray) adult mice. Each point represents one animal (18 awake mice, nine anesthetized mice).

(B) Scatterplot comparing the preferred SF at τ_{pk1} and τ_{pk2} of two-peak cells from awake (blue circles) and anesthetized (gray diamonds) mice. Black dotted line marks where the preferred SFs are equal at τ_{pk1} and τ_{pk2}. A small amount of scatter is added to the data to differentiate points at the same coordinates.

(C) Bottom, cumulative distribution of Δf_{pk} for all cells from awake (blue) and anesthetized (gray) mice. Arrows mark proportion of cells from awake and anesthetized mice with $\Delta f_{pk} \leq 0$. Red dots denote the mean Δf_{pk} values. Top, mean Δf_{pk} values for individual mice (18 awake, nine anesthetized). Statistical comparisons were done using individual mice mean values shown at top of (C).

(D) Average normalized SF response at six distinct latencies for all cells from awake mice. 30 ms (black dotted line) is used as baseline.

(E) Same as (D) but for all cells from anesthetized mice. Note that slightly different latencies were used here compared with (D) to account for the effects of anesthesia on response timing.

(F) Average normalized time-integrated SF tuning of all V1 cells from awake (blue) and anesthetized (gray) mice. Error bars denote SEM throughout. ***$p < 0.001$. c/d, cycles/degree. See also Figures S2 and S7.

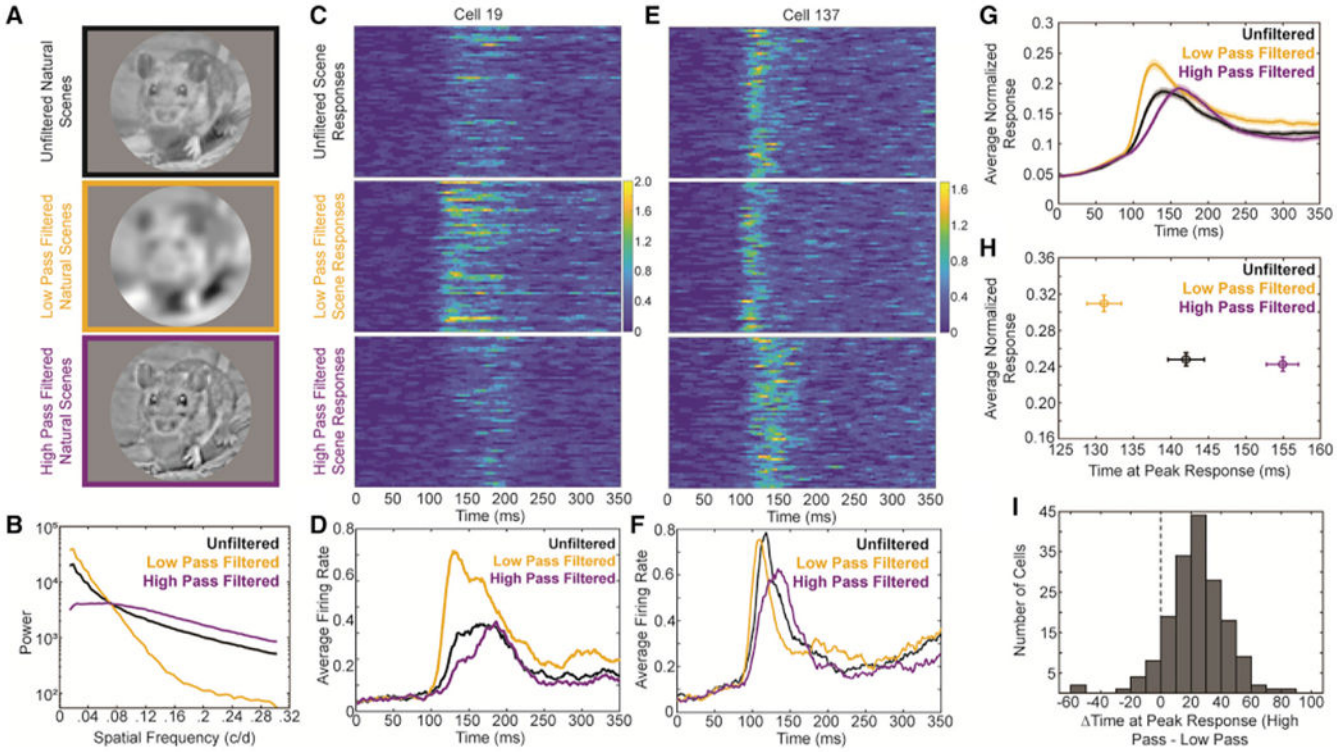

Figure 3. Awake mice process natural scenes in a coarse-to-fine manner

(A) Three variants of 60 natural scenes were shown to six awake mice; unfiltered natural scenes with $1/f$ spatial statistics (black), low-pass filtered natural scenes with attenuated high SFs (yellow), and high-pass filtered natural scenes with attenuated low SFs (purple).

(B) Average SF power spectrum of unfiltered (black), low-pass filtered (yellow), and high-pass filtered (purple) natural scenes. SEM were not included in this plot as they were smaller than the thickness of the lines. Note the $\log_{10}$ y axis.

(C) Heatmap of responses of one neuron to unfiltered (top) and low-pass (middle) or high-pass filtered (bottom) natural scenes. Scale bar denotes firing rate in spikes/s.

(D) The average firing rate of the same cell in (C) to all unfiltered (black), low-pass filtered (yellow), and high-pass filtered (purple) natural scenes.

(E–F)Another representative cell plotted in the same way as (C)–(D).

(G) Average normalized response of all 171 cells to unfiltered (black), low-pass filtered (yellow), and high-pass filtered (purple) natural scenes. Error bars represent SEM.

(H) Average normalized response (y axis) plotted against the average time at the peak response (x axis) of all cell's responses to unfiltered (black), low-pass filtered (yellow), and high-pass filtered (purple) natural scenes. Error bars represent SEM.

(I) Histogram of difference in peak response time between average high-pass and average low-pass responses from each cell. Positive values indicate that high-pass filtered image responses peak later than that of low-pass filtered images. Dotted line demarks 0. See also Figure S3.

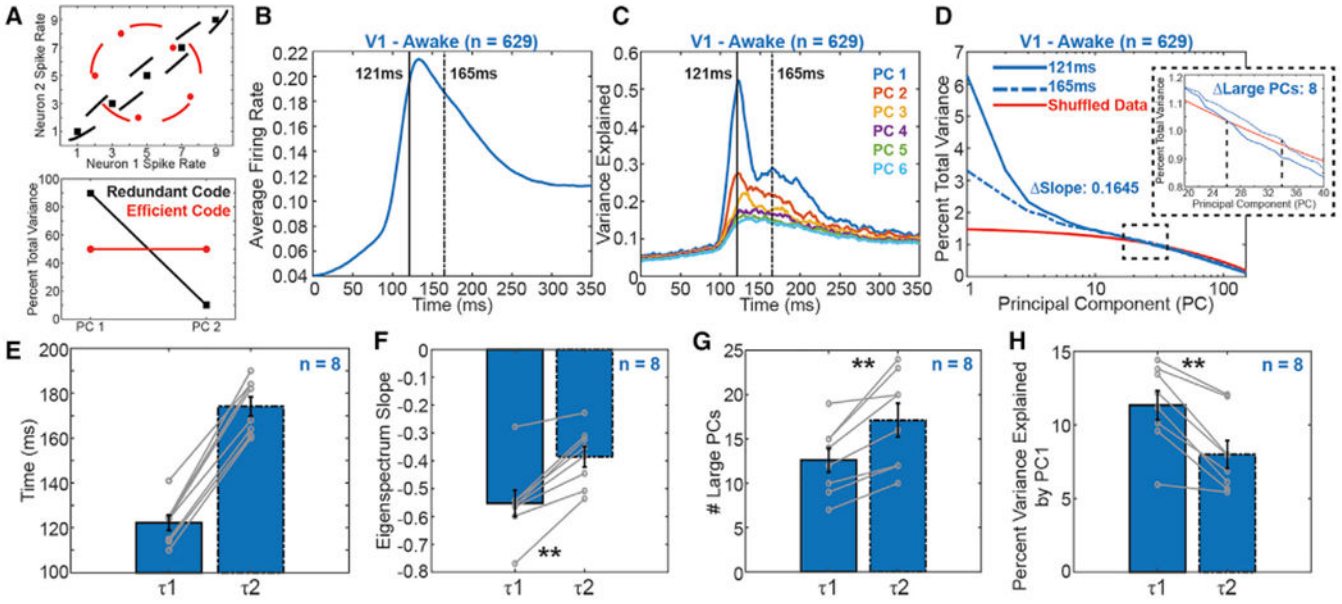

Figure 4. Coarse-to-fine SF processing reduces redundancy in neural representation of natural scenes

(A) Hypothetical two-neuron example of redundant (black) and efficient (red) neural codes. Top, schematic of responses of a redundant (black) and efficient (red) neural code to five natural scenes. Dotted lines mark the neural response manifold generated by these hypothetical neural codes. Bottom, eigenspectrum generated from these hypothetical redundant (black) and efficient (red) neural codes.

(B) Average firing rate of all cells (n = 629) to all natural scenes from V1 of eight awake mice. Solid and dotted lines mark the time points τ1 (121ms) and τ2 (165ms) used for subsequent analyses in (C)–(D).

(C) Variance explained by the first six PCs over the response period when measuring the structure of the neural response manifold generated by all 629 cells. Solid and dotted lines mark the time points τ1 (121ms) and τ2 (165ms) used for subsequent analyses in (D).

(D) Eigenspectra at 121 ms (solid line) and 165 ms (dotted line). Red line is the eigenspectrum of shuffled dataset averaged overtime. ΔSlope indicates the change in the eigenspectrum slope from τ1 (−0.49) to τ2 (−0.33). Note the $\log_{10}$ x axis. Dashed box indicates portion of eigenspectra plotted in inset. Inset, same eigenspectra but zoomed in to highlight the point at which the eigenspectra of the original data at τ1 and τ2 cross the eigenspectrum of the shuffled data. Dotted vertical lines mark the number of large PCs for τ1 and τ2. ΔLarge PCs is the difference in the number of large PCs from τ1 to τ2.

(E) Time at τ1 and τ2 for individual recordings from V1 of eight different awake mice.

(F) Eigenspectrum slope at τ1 and τ2 for individual mice (gray points connected by line). Blue bar plots indicate mean values. Error bars denote SEM.

(G) Same as (F) but for the number of large PCs at τ1 and τ2 for individual mice.

(H) Same as (F)–(G) but for the percentage of total variance explained by PC1 at τ1 and τ2 for individual mice. **p < 0.01. PC, principal component. See also Figure S4.

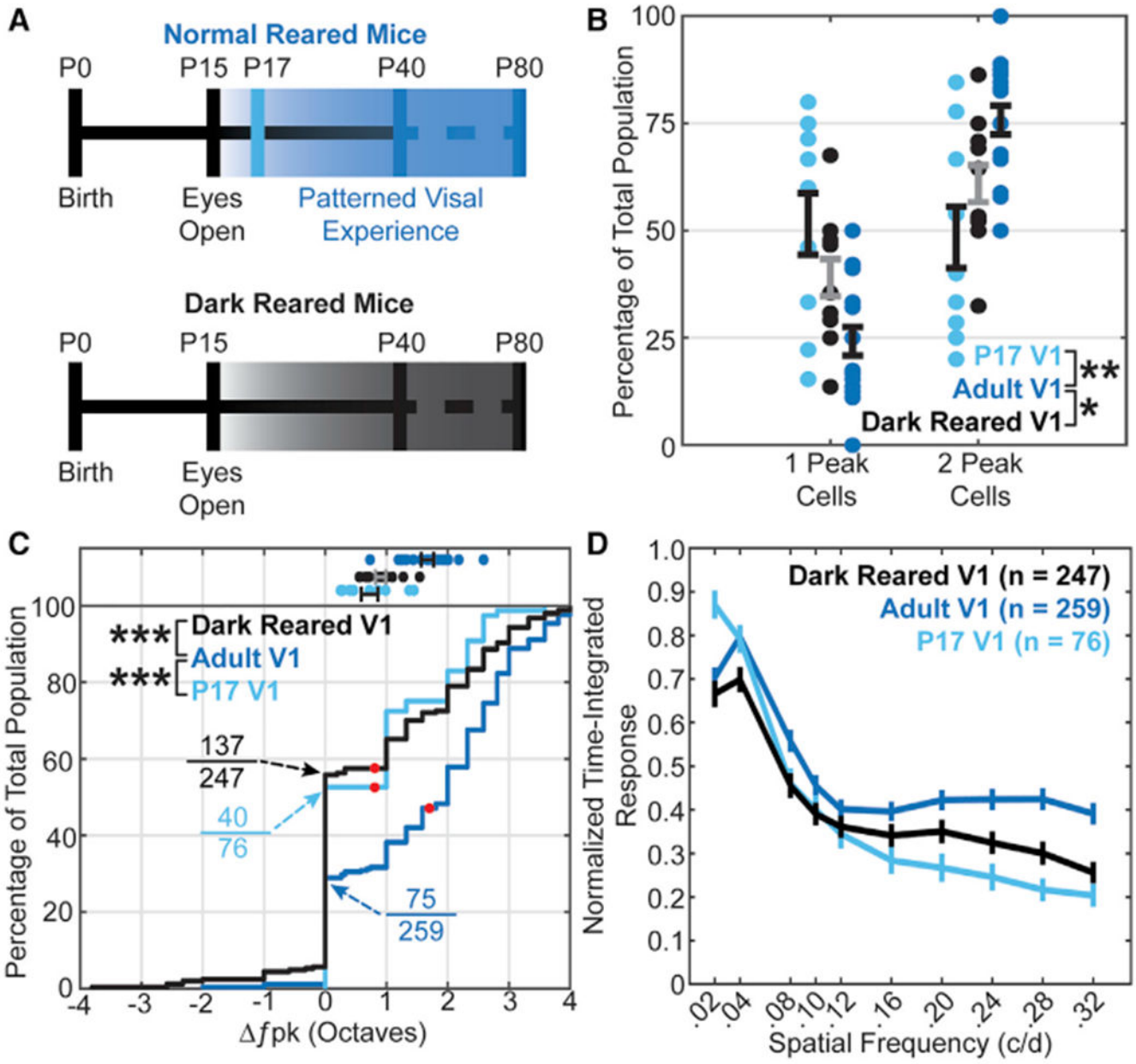

Figure 5. Experience-dependent development of coarse-to-fine SF processing

(A) Timeline of visual development in normally reared (top) and dark-reared mice (bottom).

(B) Proportion of one- and two-peak cells in V1 of normally reared adult (blue), P17 (light blue), and dark-reared adult (black) mice. Each dot represents one mouse (18 adult mice, 12 DR mice, 10 P17 mice).

(C) Bottom, cumulative distribution of Δf_{pk} for all cells from normally reared adult (blue), P17 (light blue), and dark-reared adult (black) mice. Arrows mark proportion of cells with $\Delta f_{pk} \leq 0$. Red dots denote the mean Δf_{pk} values. Top, mean Δf_{pk} values for individual mice (18 adult mice, 12 DR mice, 10 P17 mice). Statistical comparisons illustrated in legend were done using individual mice mean values shown in top of (C).

(D) Average normalized time-integrated SF tuning of the three groups. Error bars denote SEM throughout. ***$p < 0.001$. c/d, cycles/degree. See also Figures S5 and S7.

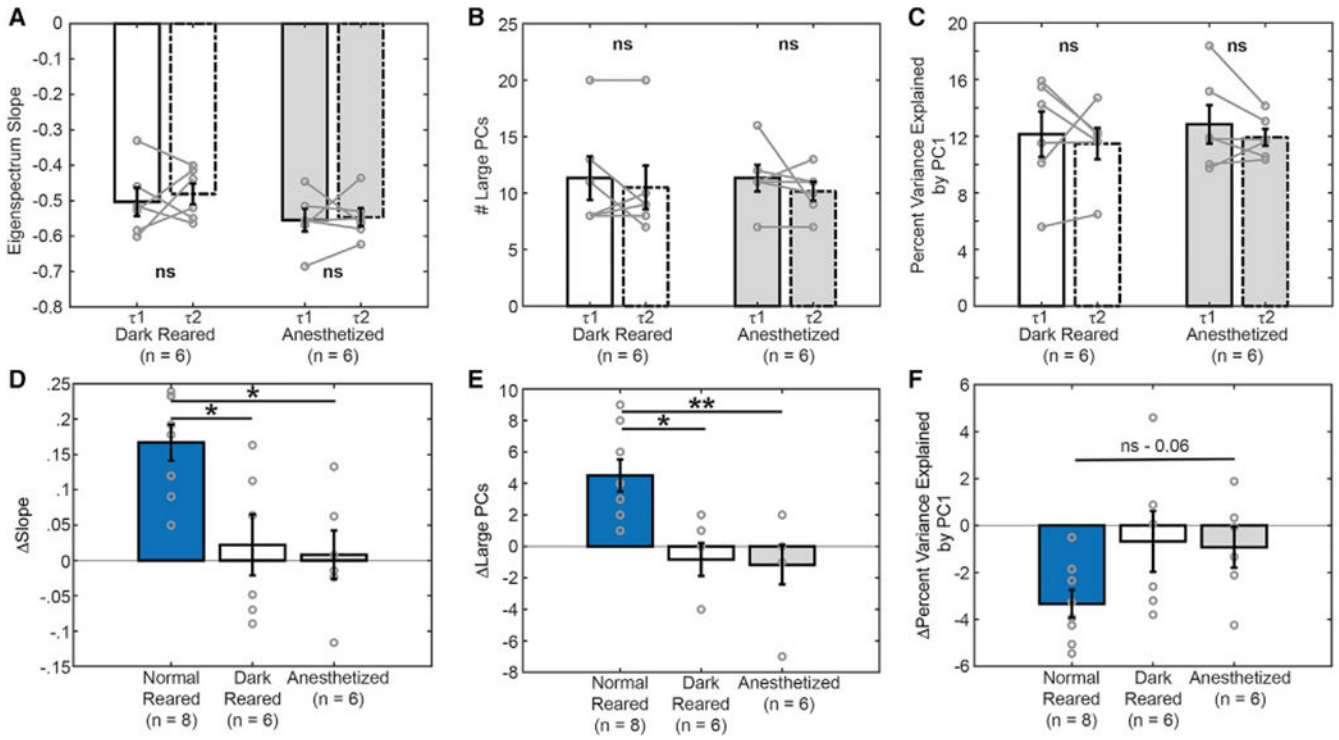

Figure 6. Disrupted redundancy reduction in natural scene responses from mice with attenuated coarse-to-fine SF processing

(A) Average eigenspectrum slope at τ1 and τ2 for individual recordings from V1 of six dark-reared mice (white bars) and V1 of six anesthetized mice (gray bars). Error bars denote SEM. Values from individual mice are marked with gray points.

(B) Same as (A) but for number of large PCs at τ1 and τ2.

(C) Same as (A)–(B) but for the percentage of total variance explained by PC1 at τ1 and τ2.

(D) Average ΔSlope for normally reared (blue), dark-reared (white), and anesthetized (gray) mice. Error bars denote SEM. Values from individual mice are marked with gray points.

(E) Same as (D) but for ΔLarge PCs.

(F) Same as (D)–(E) but for ΔPercentage of total variance explained. *p < 0.05, **p < 0.01. c/d, cycles/degree; PC, principal component; ns, not significant. See also Figure S6.

KEY RESOURCES TABLE

REAGENT or RESOURCE	SOURCE	IDENTIFIER
Chemicals, peptides, and recombinant proteins		
Carprofen	Zoetis	Cat#141-199
Chlorprothixene hydrochloride	Sigma	Cat#C1671
Vetbond	3M	Cat#70200742529
Atropine	Sigma	Cat#A0132
Urethane	Sigma	Cat#u-2500
Dexamethasone	Sigma	Cat#D4902
Metabond	Parkell	Cat#S380
Isoflurane	Covetrus	Cat#1169567761
Deposited data		
Natural Scene Database	Stringer et al., 2019	http://doi.org/10.25378/janelia.6845348.v4
Experimental models: Organisms/strains		
Mouse: C57BL/6	Bred in lab; Originally from Jackson	https://www.jax.org/strain/000664; RRID: IMSR_JAX:000664
Software and algorithms		
Psychophysics Toolbox	Psychtoolbox	http://psychtoolbox.org/docs/Psychtoolbox; RRID: SCR_002881
Matlab 2018a	MathWorks	http://www.mathworks.com/products/matlab.html; RRID: SCR_001622
MountainSort	Chung et al., 2017	https://github.com/flatironinstitute/mountainsort; RRID: SCR_017446
Intan RHD Recording Sytem	Intan Technologies	https://intantech.com/RHD_system.html; RRID: RCR_019278
Custom Written Matlab Code	This Paper	https://doi.org/10.5281/zenodo.6320882
Other		
UCLA Silicone Probes	Yang et al., 2020	https://masmanidislab.neurobio.ucla.edu/technology.html
LCD Monitor	Dell	U2417Ht
Head Holding Device	Narishige	SR-AM
Anesthesia Systems	Kent Scientific	VetFlo
Temperature Control	FHC	N/A